Accepted Manuscript

Flux blended synthesis of novel Y_2O_3:Eu^{3+} sensing arrays for highly sensitive dual mode detection of LFPs on versatile surfaces

K.N. Venkatachalaiah, H. Nagabhushana, R.B. Basavaraj, G.P. Darshan, B. Daruka Prasad, S.C. Sharma, J. Shivakumar, Lakshmi

Please cite this article as: Venkatachalaiah KN, Nagabhushana H, Basavaraj RB, Darshan GP, Daruka Prasad B, Sharma SC, Shivakumar J, Lakshmi Flux blended synthesis of novel Y_2O_3:Eu^{3+} sensing arrays for highly sensitive dual mode detection of LFPs on versatile surfaces, *Journal of Rare Earths* (2018), doi: 10.1016/j.jre.2018.04.005.

Flux blended synthesis of novel Y_2O_3:Eu^{3+} sensing arrays for highly sensitive dual mode detection of LFPs on versatile surfaces

K. N. Venkatachalaiah[1, 2], H. Nagabhushana[3, *], R.B. Basavaraj[3], G.P. Darshan[4], B. Daruka Prasad[5], S.C. Sharma[6,7], Shivakumar J[8], Lakshmi[8]

[1]*Department of Physics, Amrita School of Engineering, Amrita Vishwavidyapeetham, Amrita University, Bengaluru 560035, India*
[2]*Research and Development Center, Bharathiar University, Coimbatore 641046, India*
[3]*Prof. C.N.R. Rao Centre for Advanced Material Science, Tumakuru University, Tumakuru 572103, India*
[4]*Department of Physics, Acharya Institute of Graduate Studies, Bangalore 560107, India*
[5]*Department of Physics, B.M.S. Institute of Technology and Management, Visveswaraya Technological University affiliated, Bangalore 560064, India*
[6]*Department of Mechanical Engineering, Jain University, Advisor, Jain group of Institutions, Bangalore 560069, India*
[7]*Avinashilingam Institute for Home Science and Higher Education for Women University, Coimbatore 641043, India*
[8]*Department of Biochemistry, Meenakshi Medical College Hospital & Research Institute, Enathur, Karrapettai Post, Kanchipuram 631552, India*

Abstract

In the present communication, various fluxes blended Y_2O_3:Eu^{3+} (5 mol%) nanopowders (NPs) were successfully fabricated by solution combustion method. PXRD pattern confirms body-centered cubic structure of the prepared samples. Energy band gap (E_g) of the fabricated products was estimated and is found to be in the range of 3.13–3.32 eV. Photoluminescence (PL) emission spectra exhibit sharp and intense peaks at ~ 579, 592, 614, 657, 704 nm corresponds to $^5D_0 \rightarrow {}^7F_J$ (J = 0, 1, 2, 3 and 4) transitions of Eu^{3+} ions. Significance of fluxes for enhancing the PL emissions is extensively studied. Photometric studies of the prepared samples are located in pure red region. Optimized NPs were explored as a novel sensing agent for visualization of latent fingerprints (LFPs) on various surfaces including porous, semi-porous and non-porous surfaces followed by powder dusting technique. Various experiments including aging, temperature, scratching and aquatic fresh water treatment tests were performed to evaluate applicability of the fabricated NPs. Visualized LFPs exhibit well defined ridge details including most authenticated sweat pores are also revealed with high sensitivity, selectivity, little background hindrance and less toxicity. Aforementioned results evidence that the method and fabricated NPs can be considered to be simple, rapid and economical and provide novel sensing platform for LFPs visualization in prospective forensic applications.

Keywords: Fluxes; Photoluminescence; Latent Fingerprint; Sweat pores; Forensic applications; Rare earths

*Corresponding Author: E-mail address: bhushanvlc@gmail.com (H. Nagabhushana), Telephone No.:- +91-9663177440.

1. Introduction

Fingerprints have been extensively researched because they have unique shapes (whorl, arch and loop) and do not vary with ages. The fingerprints have several minutiae such as ridge flow (level 1), core, delta, bifurcation (level 2) and sweat pore (level 3) which are different for each individual. Therefore, fingerprints have been used as the effective trace which is an important evidence for identifying individual information and crime scenes [1–4]. However, latent fingerprints are required to develop the visualization techniques because they are invisible or barely visible to naked eyes. One of the methods for detecting the latent fingerprints is powder dusting method containing two major powder types such as metal and magnetic powders. They are effective in the development of latent fingerprints except for some problems. Firstly, they have the low contrast due to the non-fluorescence of the powders. Secondly, they have the low resolution due to their resinous polymer (starch, rosin, etc.) and colorant components. Lastly, they are harmful for user health due to their components. To settle the problems, the development of luminescent materials is demanded for replacing the metal and magnetic powders [5–8].

Recently, the application of nanopowders (NPs) has been extended to the accurate identification of latent fingerprint technology. This is because NPs are extremely small, generally 1000–10000 times smaller than a fingerprint ridge width, which ensures the excellent resolution upon detection [9]. The fingerprint constitutes one of the regular and powerful techniques for recognizing people since the ridge and furrow patterns of each print are unique and immutable [10, 11]. There are three different types of fingerprint powders: regular, metallic and luminescent. Regular fingerprint powder consists of a resinous polymer and a colorant. It is impotent to develop latent fingerprint (LFP) on challenging surfaces. Use of metallic compounds is harmful for user health because of metallic powder containing meshed metals with lead, gold and silver. Although the use of fluorescent nanomaterials, including quantum dots, carbon dots, and up conversion nanoparticles, for improving the detection limit of LFPs has been attempted, there are still concerns regarding their low detection efficiency, complicated process involved, photo bleaching, and toxicity. The visualization was restricted only level 1 and level 2 ridge characteristics due to poor fluorescent image qualities with these nanomaterials [6, 12–14]. Hence, luminescent NPs are highly required to visualize LFPs with superior sensitivity, little background hindrance, extraordinary efficiency, lesser toxicity and stress-free detection. As can be seen from **Table 1**, there is a lack of studies on aging, effect of temperature, abrasion and preservation of LFPs under aquatic conditions [6, 12, 15–20].

In the recent years, the combination of RE^{3+} ions with flux (chloride salts) emerged as a successful way to improve the PL intensity and efficiency of the phosphors [21, 22]. Fluxes play a significant role in the crystal growth and enhance the efficiency of luminescence intensity. The enhanced luminescence can be due to the local crystal field symmetry breaking around rare-earth ions [23, 24]. The addition of flux has a great influence on the ion diffusions in the solid-state reaction, particle size distribution, growth condition, crystallization process as well as the formation of target product matrix with good crystallinity [25].

Yttrium oxide (Y_2O_3) is a phosphor material which showed applications in fields viz white LED phosphors [26], commercial lighting, up-conversion materials [27, 28], transparent ceramics [29], fluorescence sensors, etc. It is an excellent host matrix for rare earth ions due to

its unique properties such as broad transparency range (0.8–2.0 mm; large band gap 5.8 eV), high refractive index (>1.9) [30]. Addition of different rare earth ions into Y_2O_3 nanostructures helps in further enhancing its emission efficiency [31]. Eu(III) acts as a red color activator, the combination of (Y_2O_3:Eu) leads to red emitting material with commercial applications and minimal degradation under applied voltages, Y_2O_3 nanostructures have been the focus of extensive research [32–35].

The present work deals with novel Y_2O_3:Eu^{3+} (5 mol%) blended with various fluxes (KCl, NH_4Cl, NaF and NH_4F) prepared by solution combustion method. The prepared samples were characterized by powder X–ray diffraction (PXRD), diffuse reflectance spectra (DRS), Fourier transform infrared (FTIR) spectra, scanning electron microscopy (SEM), transmission electron microscopy (TEM), Raman and photoluminescence studies. The optimized NPs have been extensively utilized for visualization of LFPs on various porous, semi-porous and non-porous surfaces.

2. Experimental and characterization
2.1 Chemicals
Analar grade of yttrium (III) nitrate hexahydrate: $Y(NO_3)_3 \cdot 6H_2O$ (Sigma Aldrich, 99%), europium (III) nitrate pentahydrate: $Eu(NO_3)_3 \cdot 5H_2O$ (Sigma Aldrich, 99%), urea: NH_2CONH_2 (Sigma Aldrich, 99%); potassium chloride: KCl (Sigma Aldrich, ≥ 99%); ammonium chloride: NH_4Cl (Sigma Aldrich, ≥ 99.5%); sodium fluoride: NaF (Sigma Aldrich, ≥ 99.5%); ammonium fluoride: NH_4F (Sigma Aldrich, ≥ 99.5%) and double distilled water.

2.2 Synthesis of flux blended Y_2O_3:Eu^{3+} NPs
3.83 g of yttrium nitrate, 0.0428 g of europium nitrate and 0.6 g of urea were taken in a 350 mL Pyrex dish, dissolved in double distilled water and mixed homogeneously using magnetic stirrer for ~ 20–30 min. Then the resultant precursor solution was introduced into preheated muffle furnace maintained at 450 ± 10 $^{\circ}$C. Within ~ 15–20 min the solution underwent self-ignition and metal nitrates decomposed with smoldering. The resulting powder was crushed and calcined at ~700 $^{\circ}$C for ~ 3 h. Similar procedure was repeated using various fluxes KCl, NH_4Cl, NaF and NH_4F (1 wt%). Finally obtained NPs were used for further characterizations.

2.3 Visualization of LFPs using optimized Y_2O_3:Eu^{3+} (5 mol%):NH_4F (1 wt%) NPs
Various non-porous surfaces used in the present study were thoroughly cleaned by alcohol to ensure no unintended LFPs was deposited. After that the cleaned fingers of the donar were pressed against various surfaces including porous, semi-porous and non-porous surfaces by smooth rolling. The bare LFPs were treated with fresh water aquatic condition with various aging and later stained by the optimized Y_2O_3:Eu^{3+} (5 mol%):NH_4F (1 wt%)NPs by a soft feather brush with light brushing action. To evaluate LFPs development technique the physical scratch test is carried out by sealing adhesive tape on tothe developed FPs and then peeling off from the surface. In addition, effect of temperature (30, 35, 40, 50 $^{\circ}$C) was also performed on LFPs stored for ~ 10 min. Finally, the developed LFPs were photographed *in situ* using a 50 mm f/2.8 G, ED lens Nikon D3100/AF-S digital camera under normal and 254 nm UV lamp.

2.4 Characterization
The Philips powder X-ray diffractometer (Shimadzu-7000) with Ni filtered Cu Kα radiation was used to study the powder X-ray diffraction (XRD) studies. The Perkin Elmer (Spectrum RXIFTIR) spectrometer was used to carry out FTIR studies. Morphological (SEM and TEM) analysis were carried out by a Hitachi 3000 table top scanning electron microscope and a Hitachi H-8100 accelerating voltage up to 200 KV, LaB_6 filament equipped with EDS (Kevex sigma TM Quasar, USA). The Jobin Yvon Horiba LABRAM-HR-Visible micro Raman system was used

for Raman studies with He-Ne laser (~ 632.8 nm) as the source. Diffuse reflectance (DR) spectra of all the prepared NPs were recorded by PerkinElmer (Lambda-35) spectrophotometer. PL studies were performed by a Horiba (JobinYuvon) spectrometer having slit width of 5 nm.

3. Results and discussion

PXRD profiles of Y_2O_3:Eu^{3+} (5 mol%) and Y_2O_3:Eu^{3+} (5 mol%), M (M=KCl, NaF, NH_4Cl and NH_4F (1 wt%)) NPs, are shown in Fig.S1 (a).Detailed discussion about the crystallite property was discussed in the supplementary section. The average crystallite sizes of prepared Y_2O_3:Eu^{3+} (5 mol%) and Y_2O_3:Eu^{3+} (5 mol%), M (M=KCl, NaF, NH_4Cl and NH_4F (1 wt%)) NPs were estimated and found to be 45, 38, 43, 52, 47 and 56 nm, respectively.

Fig. 1 depicts the morphologies of Y_2O_3:Eu^{3+} (5 mol%) KCl, NaF, NH_4Cl and NH_4F (1 wt%) blended Y_2O_3:Eu^{3+} NPs. Irregular shaped particles with large pores were observed in Y_2O_3:Eu^{3+} (5 mol%) NPs (Fig.1(a)). However, KCl and NH_4Cl blended Y_2O_3:Eu^{3+} (5 mol%) NPs exhibit sponge-like structures with large voids. Whereas NaF blended samples exhibit irregular shaped particles without any porosity. Spherical shaped particles with smooth surface were observed in NH_4F blended Y_2O_3:Eu^{3+} (5 mol%) NPs (Fig. 1(e)). These results clearly evidence that the fluoride fluxes in particular NH_4F facilitate to fabricate well defined shaped particles with high purity and good chemical homogeneity owing to rapid evaporation or decomposition properties of NH_4F flux that lead to fast nucleation.

TEM images of Y_2O_3:Eu^{3+} (5 mol%) and Y_2O_3:Eu^{3+} (5 mol%), M (M=KCl, NaF, NH_4Cl and NH_4F (1 wt%)) NPs are as shown in Fig. 2(a–e). Well defined spherical shaped Y_2O_3:Eu^{3+} (5 mol%), NH_4F (1 wt%) NPs are also evidenced in TEM results (Fig. 2(e)). The HRTEM image and SAED patterns of Y_2O_3:Eu^{3+} (5 mol%), NH_4F (1 wt%) NPs are shown in Fig.2 (f, g). The inter-planar distance 'd' between the planes corresponding to (222) plane is found to be ~ 0.24 nm. The SAED pattern confirms the crystalline nature and circles are matched with the (hkl) planes of the PXRD results.

Fig. 3(a) shows DR spectra (DRS) of Y_2O_3:Eu^{3+} (5 mol%) NPs with and without the use fluxes. The spectra exhibit characteristic absorption peaks at 393, 464 and 557 nm attributed to $^7F_0 \rightarrow {}^5L_6$, $^5D_2$ and $^5D_1$ transitions of Eu^{3+} ions, respectively[36]. Further, Kubelka-Munk relation was used to estimate energy band gap (E_g) of the prepared samples by analyze the DR spectra as follows:

$$F(R_\infty) = \frac{(1-R_\infty)^2}{2R_\infty} \text{-------------------- (2)}$$

$$hv = \frac{1240}{\lambda} \text{-------------------- (3)}$$

where R_∞ is reflection coefficient of the sample, λ the absorption wavelength, and h Planck's constant. From the plots of $\left[F(R_\infty)hv\right]^{1/2}$ versus photon energy (Fig. 3(b)), the E_g values of prepared Y_2O_3:Eu^{3+} (5 mol%), Y_2O_3:Eu^{3+} (5 mol%), M (M=KCl, NaF, NH_4Cl and NH_4F (1 wt%)) NPs were estimated and found to be ~ 3.32, 3.27, 3.16, 3.13 and 3.30 eV respectively. The variation in the E_g values is mainly due to creation of sub-structure with co-doping which may lead to oxygen vacancies.

FTIR spectra of Y_2O_3:Eu^{3+} (5 mol%) and Y_2O_3:Eu^{3+} (5 mol%), M (M=KCl, NaF, NH_4Cl and NH_4F (1 wt%)) NPs were recorded and the results are shown in Fig. 3(c). The strong

absorption peak centered at ~ 568 cm^{-1} is owing to Y–O lattice vibration. The peaks at ~ 863 and 1075, 1403, 1563 cm^{-1} were due to C–O bond bending and stretching vibration, respectively. The observed peaks are due to carbon contents or CO_2 absorption from the ambient atmosphere. The broad absorption band at ~ 3542 cm^{-1} corresponds to O-H stretching vibrations[37].

Fig. 3(d) displays Raman spectra of Y_2O_3:Eu^{3+} (5 mol%) NPs prepared with and without fluxes. The spectra exhibit several peaks recorded at ~ 132, 164, 195, 318, 333, 378, 468, 603, 705 and 741 cm^{-1}. The intense peaks centered at ~ 378 and 705 cm^{-1} are associated to characteristic of cubic structure and dopant Eu^{3+} ions Y_2O_3 host matrix. The existence of these peaks in NPs with and without fluxes indicates that the cubic phase has been retained on doping. The intensity of these peaks related to with flux is found to be enhanced[38].

Fig. 4(a) shows the PL excitation spectra of Y_2O_3:Eu^{3+} (5 mol%) and Y_2O_3:Eu^{3+} (5 mol%), M (M=KCl, NaF, NH_4Cl and NH_4F (1 wt%)) NPs under 612 nm emission wavelength. The excitation spectra of the prepared samples exhibit broad intense peak at ultraviolet region (225–300 min) owing to O^{2-} to Eu^{3+} charge transfer band (CTB) attributed to the electronic transition from the 2p orbital of O^{2-} to the empty 4f orbital of Eu^{3+} ions. The zero phonon line spectra are shown in Fig. 4(b). The existence of CTB specifies covalent nature of Eu–O bond. The remaining peaks observed in the spectra are mainly attributed to f-f transitions of Eu^{3+} activator. PL emission spectra of Y_2O_3:Eu^{3+} (5 mol%) and Y_2O_3:Eu^{3+} (5 mol%), M (M=KCl, NaF, NH_4Cl and NH_4F (1 wt%)) NPs excited at 396 nm wavelength are shown in Fig. 4(c). The spectra exhibit sharp and intense peaks at ~ 579, 592, 614, 657, 704 nm wavelengths corresponding to $^5D_0 \rightarrow {}^7F_J$ (J = 0, 1, 2, 3 and 4) transitions of Eu^{3+} ions. The $^5D_0 \rightarrow {}^7F_1$ and $^5D_0 \rightarrow {}^7F_2$ transitions are due to magnetic and electric dipole (MD and ED) transitions of Eu^{3+} ions, respectively[39]. Moreover, MD transition may not depend on host lattice symmetry, while hypersensitive ED transition mainly depends on the host lattice. In our present work, ED transition (614 nm) is predominant as compared to MD transition (592 nm) due to the effective substitution of Eu^{3+} ions in Y_2O_3 sites without inversion center and lower symmetry of the crystal field.

Asymmetry ratio (A_{21}) between the peaks at ~ 614 and 592 nm was estimated by the area under the peaks, as follows [40]:

$$A_{21} = \frac{\int\limits_{600}^{620} A_2 \, d\lambda}{\int\limits_{580}^{605} A_1 \, d\lambda} \text{-------- (4)}$$

where, subscript "1" and "2" denote transitions of $^5D_0 \rightarrow {}^7F_1$ and $^5D_0 \rightarrow {}^7F_2$, respectively. The maximum value of A_{21} is observed in Y_2O_3:Eu^{3+} (5 mol%), NH_4F (1 wt%) NPs, which suggest an enhancement in red color. The variation of PL intensity with fluoride fluxes was investigated in detail, as shown in Fig.4 (d).The enhanced PL intensity (approximately 3-fold) is observed for Y_2O_3:Eu^{3+} (5 mol%), NH_4F (1 wt%) NPs, which may due to crystal field splitting and crystal symmetry distortion (Fig.4 (d)).

The chromaticity co-ordinates of the prepared samples were estimated as per regulations of the Commission Internationale de I 'Eclairage (CIE)[41]. The CIE chromaticity diagram of prepared samples are shown in Fig. 4(e). From the figure, it is evident that the CIE co-ordinates are located in the pure red region. Correlated color temperature (CCT) can be estimated by Planckian locus, which is only a small portion of the (x, y) chromaticity diagram and there exist many operating points outside the Planckian locus. If the co ordinates of a light source do not fall

on the Planckian locus, the CCT was used to define the color temperature of a light source. CCT is calculated by transforming the (x, y) coordinates of the light source to (u_0, v_0) by using the equations.

$$u' = \frac{4x}{-2x + 12y + 3} \text{-------- (5)}$$

$$v' = \frac{9y}{-2x + 12y + 3} \text{-------- (6)}$$

$$CCT(x, y) = -449n^3 + 3525n^2 - 6823.3n + 5520.33 \text{---------- (7)}$$

where, $n = (x - 0.3320)/(y - 0.1858)$. By determining the temperature of the closest point of the Planckian locus to the light source on the (u_0, v_0) uniform chromaticity diagram is shown in Fig. 4(f). The lamps with a CCT value below 3200 K are usually considered as "warm" light sources, while those with a CCT above 4000 K are considered as "cool" in appearance [42]. The estimated CCT values of the prepared samples were located in range between ~ 2000 – 3000 K (Fig. 4(f)). In addition, color purity of the optimized sample is calculated using the following formula[43]:

$$\text{color purity} = \frac{\sqrt{(x_s - x_i)^2 + (y_s - y_i)^2}}{\sqrt{(x_d - x_i)^2 + (y_d - y_i)^2}} \times 100\% \text{--------------- (8)}$$

where (x_s, y_s) and (x_d, y_d) are the coordinates of a sample point and dominant wavelength respectively and (x_i, y_i) are the coordinates of the illuminate point. The color purity of the optimized samples was calculated and found to be ~ 88%.

In order to explore the effectiveness of the prepared samples, the LFPs are visualized by staining Y_2O_3:Eu^{3+} (5 mol%) NPs prepared with and without fluxes on glass and aluminium foil surface under 254 nm UV light (Figs. 5 & 6). From the figures, it is clear that a high quality well defined ridge details (level I – III) are visualized after stained by NH_4F assisted Y_2O_3:Eu^{3+} (5 mol%) NPs as compared to the other samples. It evidenced that the optimized Y_2O_3:Eu^{3+} (5 mol%), NH_4F NPs is explored as a labeling marker for further studies. In addition, the selectivity of the optimized sample for visualization of LFPs, conventionally used Fe_2O_3 and TiO_2 staining powders were used as control. It is evident that Fe_2O_3 and TiO_2 powders could not be able to visualize LFPs on aluminium foil (Fig.7). However, LFPs visualized by staining optimized sample clearly revealed friction ridges with well defined sharp edges under both normal and UV 254 nm light. The obtained results also reveal optimized Y_2O_3:Eu^{3+} (5 mol%), NH_4F NPs can be used as an efficient labeling agent for identification of individuals due to their enhanced luminosity and nano-regime (Fig.7).

Further, a series of experiments were performed for evaluation of the optimized NPs for visualization of LFPs on non-porous surfaces such as spatula, highlighter, glass, coin, compact disc and goggle under normal and UV 254 nm light**.** Fig.S2, Fig.S3 and their explanation in the supplementary section give the effectiveness of this method on various surfaces and the visualization of level III ridges. Generally, the porous surfaces, namely paper, cardboard and wood, are rapid absorptive of LFPs residues after deposition. Water-soluble chemical constituents of LFPs such as amino acids, urea and chlorides are absorbed within few seconds and as water evaporates constituents are stay on the surface for longer period. To boost practical advantages of the optimized samples, LFPs were developed on complicated and high color

6

background porous playing cards and crushed aluminium foil surface under UV 254 nm light (Fig.8). The visualized FPs exhibits well defined ridge characteristics without background hindrance, indicating the sensitivity of the prepared sample for effective identification of individuals during crime spot investigation.

Further, the semi-porous surface lies in between the porous and non-porous surfaces. We encountered most neglected semi-porous surfaces such as various fruits and vegetables namely, brinjal, capsicum, cucumber, green apple, watermelon and papaya visualized under normal and 254 nm UV (Fig.S4).The details of ridge observations were discussed in the supplementary section.Generally conditions which affect the visualization of LFPs include nature of surface, time elapsed since deposition, environmental factors (air circulation, dust, humidity, light exposure, precipitation, temperature, ultraviolet rays) enhancement techniques, etc. Further, chemical constituents of LFPs considerably change due to surface reactions, diverse decomposition, and oxidative mechanisms. In general, the LFPs compositions can be classified as: (i) the initial composition, at deposition chemical constituents present in fingertip is transferred to the surface and (ii) the aged composition, containing the existing initial constituents and degradation products [44, 45]. A little research has been required to identify the changes between the initial and aged compositions and rate of change with time. Hence, a series of aging tests have been performed on various surfaces including glass slide and cup, highlighter, compact disc, aluminium foil and playing card under UV 254 nm light. As shown in Fig. 9, the visualization sensitivity gradually decreased with prolonged aging of the FPs. In addition, LFPs aged upto 30 d could also visualize with well defined ridge edges, signifies the sensitivity of the prepared sample.LFPs on glass surface stored at different temperatures stained by optimized NPs were discussed in the supplementary section.In addition, aquatic tests were also carried out by treating bare LFPs with fresh water upto 7 d. The results evidence that the duration of submersion in fresh water would not affect FPs quality for even longer duration (7 d) (Fig. 10). This could be of practical importance during examination of such evidences.Further, a series of physical scratch tests were performed on various surfaces and we investigated the effect of external abrasions which can destroy LFPs as discussed in the supplementary section (Fig.S6).

4. Conclusions

In summary, Y_2O_3:Eu^{3+} (5 mol%) NPs prepared using various fluxes show enhanced PL emission compared to without fluxes. Nano regime was confirmed by TEM and PXRD characterization results. NH_4F flux blended NPs show the highest PL intensity among the used fluxes. These samples can be used effectively as a novel colorimetric sensing assay for the visualization of LFPs on various complicated and neglected surfaces. The calculated CIE coordinates for the optimized samples are found to be (0.65, 0.35) under NUV excitation, which are close to the coordinates of NTSC standard for red color. The visualized LFPs exhibits high efficiency and high sensitivity due to rapid development procedure and without any background interference. The duration of submersion in fresh water would not affect LFPs quality even for longer duration. The scratched LFPs also exhibit clear and well defined ridge details. The prepared NPs can be a potential candidate for WLED and forensic applications.

References

[1] Muniswamy D, Nagabhushana H, Basavaraj RB, Darshan GP, Daruka Prasad B. Surfactant-assisted $BaTiO_3:Eu^{3+}@SiO_2$ core–shell superstructures obtained by ultrasonication method: Dormant fingerprint visualization and red component of white light-emitting diode applications. *ACS Sustainable Chem Eng.* 2018; 6: 5214.

[2] Basavaraj RB, Nagabhushana H, Darshan GP, Daruka Prasad B, Rahul M, Sharma SC, et al. Red and green emitting CTAB assisted $CdSiO_3:Tb^{3+}/Eu^{3+}$ nanopowders as fluorescent labeling agents used in forensic and display applications. *Dyes Pigm.* 2017;147:364.

[3] Darshan GP, Premkumar HB, Nagabhushana H, Sharma SC, Daruka Prasad B, Prashantha SC, et al. Superstructures of doped yttrium aluminates for luminescent and advanced forensic investigations. *J Alloys Compd.* 2016;686:577.

[4] Basavaraj RB, Nagabhushana H, Darshan GP, Daruka Prasad B, Sharma SC, Venkatachalaiah KN. Ultrasound assisted rare earth doped Wollastonite nanopowders: Labeling agent for imaging eccrine latent fingerprints and cheiloscopy applications. *J Ind Eng Chem.* 2017;51:90.

[5] Sharma V, Das A, Kumar V, Ntwaeaborwa OM, Swart HC, Potential of $Sr_4Al_{14}O_{25}:Eu^{2+}$, Dy^{3+} inorganic oxide-based nanophosphor in Latent fingermark detection. *J Mater Sci.* 2014;49:2225.

[6] Chen H, Ma RL, Chen Y, Fan LJ. Fluorescence development of latent fingerprint with conjugated polymer nanoparticles in aqueous colloidal solution. *ACS Appl Mater Interfaces.* 2017;9:4908.

[7] Park SJ, Kim JY, Yim JH, Kim NY, Lee CH, Yang SJ, et al. The effective fingerprint detection application using $Gd_2Ti_2O_7:Eu^{3+}$ nanophosphors. *J Alloys Compd.* 2018;741:246.

[8] Rohini BS, Nagabhushana H, Darshan GP, Basavaraj RB, Sharma SC, Amudha P, et al. Multifunctional applications of self-assembled 3D $CeO_2:Cr^{3+}$ hierarchical structures synthesized via ultrasound assisted sonochemical route. *J Alloys Compd.* 2017;724:909.

[9] Sodhi GS, Kaur J, Powder method for detecting LFPs: A review. *Forensic Sci Int.* 2001;120: 172.

[10] Wang J, Wei T, Li XY, Zhang BH, Wang JX, et al. Near-infrared-light-mediated imaging of latent fingerprints based on molecular recognition. *Angew Chem Int Ed.* 2014;53:1616.

[11] Wang J, Ma QQ, Liu HY, Wang YQ, Shen HJ, Hu XX. Time-gated imaging of latent fingerprints and specific visualization of protein secretions via molecular recognition. *Anal Chem.* 10.1021/acs.analchem.7b03003.

[12] Kim YJ, Jung HS, Lim JY, Ryu SJ, Lee JK. Rapid imaging of latent fingerprints using biocompatible fluorescent silica nanoparticles. *Langmuir.* 2016;32:8077.

[13] Chen J, Wei JS, Zhang P, Niu XQ, Zhao W, Zhu ZY, et al. Red-emissive carbon dots for fingerprints detection by spray method: Coffee ring effect and unquenched fluorescence in drying process. *ACS Appl Mater Inter.* 2017;9:18429.

[14] Venkataravanappa M, Basavaraj RB, Darshan GP, Daruka Prasad B, Sharma SC, HemaPrabha P, et al., Multifunctional Dy (III) doped di-calcium silicate array for boosting display and forensic applications, *J. Rare Earths.*https://doi.org/10.1016/j.jre.2017.11.013.

[15] Wang M, Zhu Y, Mao CB. Synthesis of NIR-responsive $NaYF_4$:Yb,Er upconversion fluorescent nanoparticles using an optimized solvothermal method and their applications in enhanced development of latent fingerprints on various smooth substrates. *Langmuir.* 2015;31:7084.

[16] Park JY, Yang HK, Novel red-emitting $Y_4Zr_3O_{12}$:Eu^{3+} nanophosphor for latent fingerprint technology. *Dyes Pigm.* 2017;141:348.

[17] Wang M, Li M, Yu A, Wu J, Mao C. Rare earth fluorescent nanomaterials for enhanced development of latent fingerprints. *ACS Appl Mater Interfaces.* 2015;7:28110.

[18] Chen YH, Kuo SY, Tsai WK, Ke CS, Liao CH, Chen CP, et al. Dual colorimetric and fluorescent imaging of latent fingerprints on both porous and nonporous surfaces with near-infrared fluorescent semiconducting polymer dots. *Anal Chem.* 2016;88:11616.

[19] Yu YL, Yan L, Xia ZN. Non-toxic luminescent Au Nanoclusters@Montmorillonitenano composites powders for latent fingerprint development. *RSC Adv.* 2017;7:50106.

[20] Wang JK, He N, Zhu YL, An ZB, Chen P, Grimes CA, et al. Highly-luminescent Eu, Sm, Mn-doped CaS up/down conversion nano-particles: application to ultra-sensitive latent fingerprint detection and in vivo bioimaging. *Chem. Commun.* 2018;54:591.

[21] Swati G, Bishnoi S, Singh P, Rajesh B, Kumar G, Seth P, et al. Novel flux-assisted synthesis for enhanced afterglow properties of $(Ca,Zn)TiO_3$:Pr^{3+} phosphor. *J Alloys Compd.* 2017;698:930.

[22] Jiang ZQ, Gou J, Min YT, Huang CH, Lv WY, Yu XC, et al. Crystal structure and luminescence properties of a novel non-rare-earth activated blue-emitting garnet phosphor $Ca_4ZrGe_3O_{12}$: Bi^{3+} for n-UV pumped light-emitting diodes. *J. Alloy Compd.* 2017;727:63.

[23] Vishwakarma AK, Jayasimhadri M, Significant enhancement in photoluminescent properties via flux assisted Eu^{3+} doped $BaNb_2O_6$ phosphor for white LEDs. *J Alloys Compd.* 2016;683: 379.

[24] Cao RP, Chen G, Yu XG, Tang PJ, Luo ZY, Guo SL, et al. Enhanced photoluminescence of $CaTiO_3$:Sm^{3+} red phosphors by Na^+, H_3BO_3 added. *Mater Chem Phys.* 2016;171:222.

[25] Chen DQ, Zhou Y, Xu W, Zhong JS, Jia ZG, Xiang WD. Enhanced luminescence of Mn^{4+}:$Y_3Al_5O_{12}$ red phosphor via impurity doping. *J Mater Chem C.* 2016;4:1704.

[26] Dai QL, Foley ME, Breshike CJ, Lita A, Strouse GF. Ligand-passivated Eu:Y_2O_3 nanocrystals as a phosphor for white light emitting diodes. *J Am Chem Soc.* 2011;133: 15475.

[27] Liang HJ, Zheng YD, Chen GY, Wu L, Zhang ZG, Cao WW, Enhancement of upconversion luminescence of Y_2O_3:Er^{3+} nanocrystals by codoping Li^+–Zn^{2+}. *J Alloys Compd.* 2011;509: 409.

[28] Qin XP, Zhou GH, Yang H, Yang Y, Zhang J, Wang SW, Synthesis and upconversion luminescence of monodispersed, submicron-sized Er^{3+}: Y_2O_3 spherical phosphors. *J Alloys Compd.* 2010;493:672.

[29] Wang CN, Li Y, Zhang WP, Yin M, Effect of acidity on microstructure and spectroscopic properties of Y_2O_3:Eu^{3+} powders and ceramics. *Spectrochim Acta Part A.* 2010;75:8.

9

[30] Lefever RA, Matsko J. Transparent yttrium oxide ceramics. Mater Res Bull. 1967;2:865.

[31] Ferrari JL, Lima KO, Pecoraro E, Ferreira RAS, Carlos LD, Gonçalves RR. Color tunability of intense upconversion emission from Er^{3+}–Yb^{3+} co-doped SiO_2–Ta_2O_5 glass ceramic planar waveguides. *J Mater Chem.* 2012;22:9901.

[32] Shionoya S, Yen W. Phosphor. New York: Handbook CRC Press, 1999.

[33] Yang J, Quan ZW, Kong DY, Liu XM, Lin J. Y_2O_3:Eu^{3+} microspheres: Solvothermal synthesis and luminescence properties. *Cryst Growth Des.* 2007;7:730.

[34] Wang HY, Wang Y, Yang Y, Li X, Wang C. Photoluminescence properties of the rare-earth ions in the TiO_2 host nanofibers prepared via electrospinning. *Mater Res Bull.* 2009;44: 408.

[35] Yang L, Tang YH, Chen XH, Li Y, Cao XL. Synthesis of Eu^{3+} doped Y_2O_3 nanotube arrays through an electric field-assisted deposition method. *Mater Chem Phys.* 2007;195:101.

[36] Zhang XG, Chen MY, Zhang JL, Qin XZ, Gong ML. Photoluminescence studies of high-efficient red-emitting $K_2Y(WO_4)(PO_4)$:Eu^{3+} phosphor for NUV LED. *Mater Res Bull.* 2016;73:219.

[37] Ivanov MG, Kynast U, Leznin M. Eu^{3+} doped yttrium oxide nano-luminophores from laser synthesis. *J Lumin.* 2016, 169: 744.

[38] Kumar Y, Pal M, Herrera M, Mathew X. Effect of Eu ion incorporation on the emission behavior of Y_2O_3 nanophosphors: A detailed study of structural and optical properties. *Opt Mater.* 2016;60:159.

[39] Lo C, Duh J, Chiou B, Peng C, Ozawa L. Synthesis of Eu^{3+}-activated yttrium oxysulfide red phosphor by flux fusion method. *Mater Chem Phys.* 2001;71:179.

[40] Kang HS, Kang YC, Jung KY, Park SB. Eu-doped barium strontium silicate phosphor particles prepared from spray solution containing NH4Cl flux by spray pyrolysis. *Mater Sci Eng B.* 2005;121:81.

[41] Kim JS, Park YH, Kim SM, Choi JC, Park HL. Temperature-dependent emission spectra of M_2SiO_4:Eu^{2+} (M=Ca, Sr, Ba) phosphors for green and greenish white LEDs. *Solid State Commun.* 2005;133:445.

[42] Ye S, Xiao F, Pan YX, Ma YY, Zhang QY. Phosphors in phosphor-converted white light-emitting diodes: Recent advances in materials, techniques and properties. *Mater Sci Eng R.* 2010;71:1.

[43] Liu WR, Huang CH, Wu CP, Chiu YC, Yeha YT, Chen TM. High efficiency and high color purity blue-emitting $NaSrBO_3$:Ce^{3+} phosphor for near-UV light-emitting diodes. *J Mater Chem.* 2011;21:6869.

[44] Rae L, Gentles D, Farrugi KJ. An investigation into the enhancement of fingermarks in blood on fruit and vegetables. *Sci. Just.* 2013;53:321.

[45] Cadd S, Islam M, Manson P, Bleay S. Fingerprint composition and aging: A literature review. *Sci. Just.* 2015;55:219.
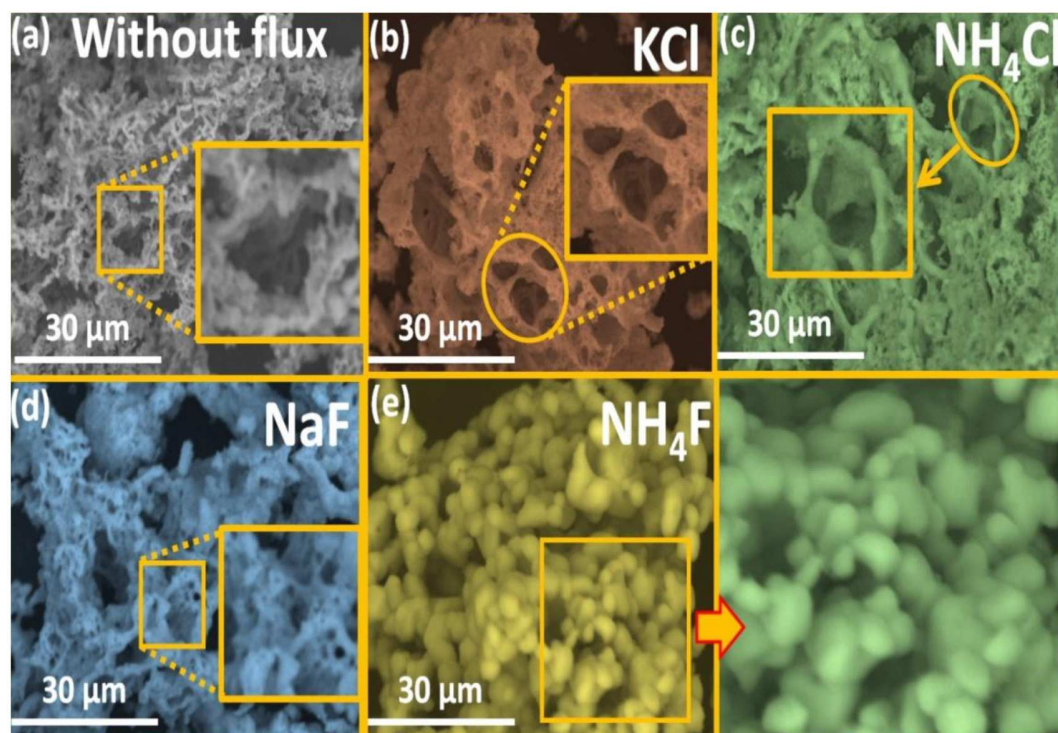
Figures

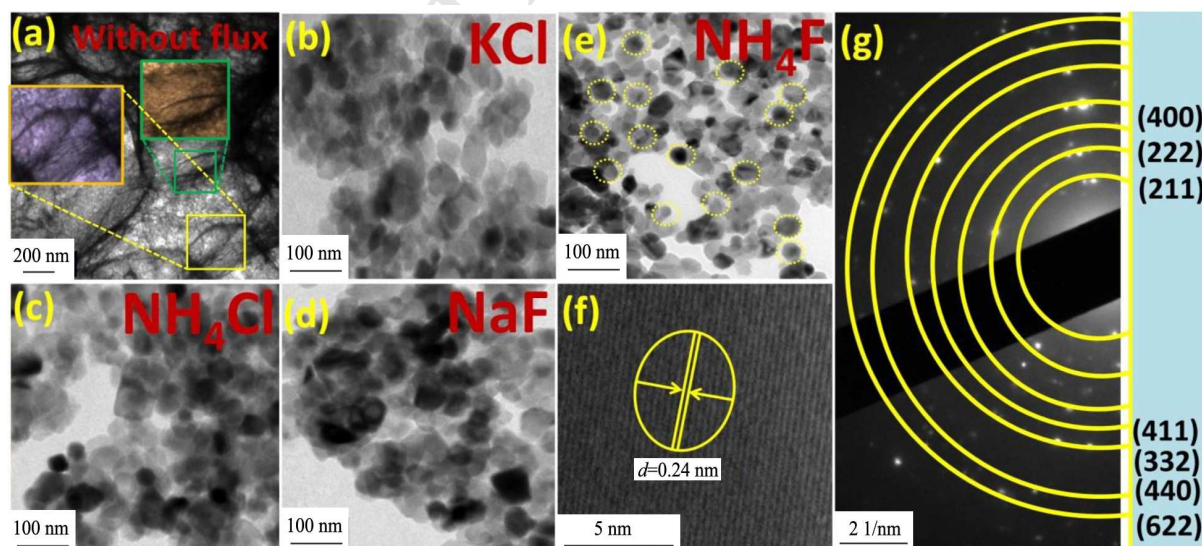Fig.1. SEM micrographs of Y_2O_3:Eu^{3+} (5 mol%) NPs without and with fluxes.

Fig.2 (a-e) TEM images of Y_2O_3:Eu^{3+} (5 mol%) NPs without and with fluxes; (f) HRTEM and (g) SAED patterns of Y_2O_3:Eu^{3+} (5 mol%), NH_4Cl (1 wt%) NPs.
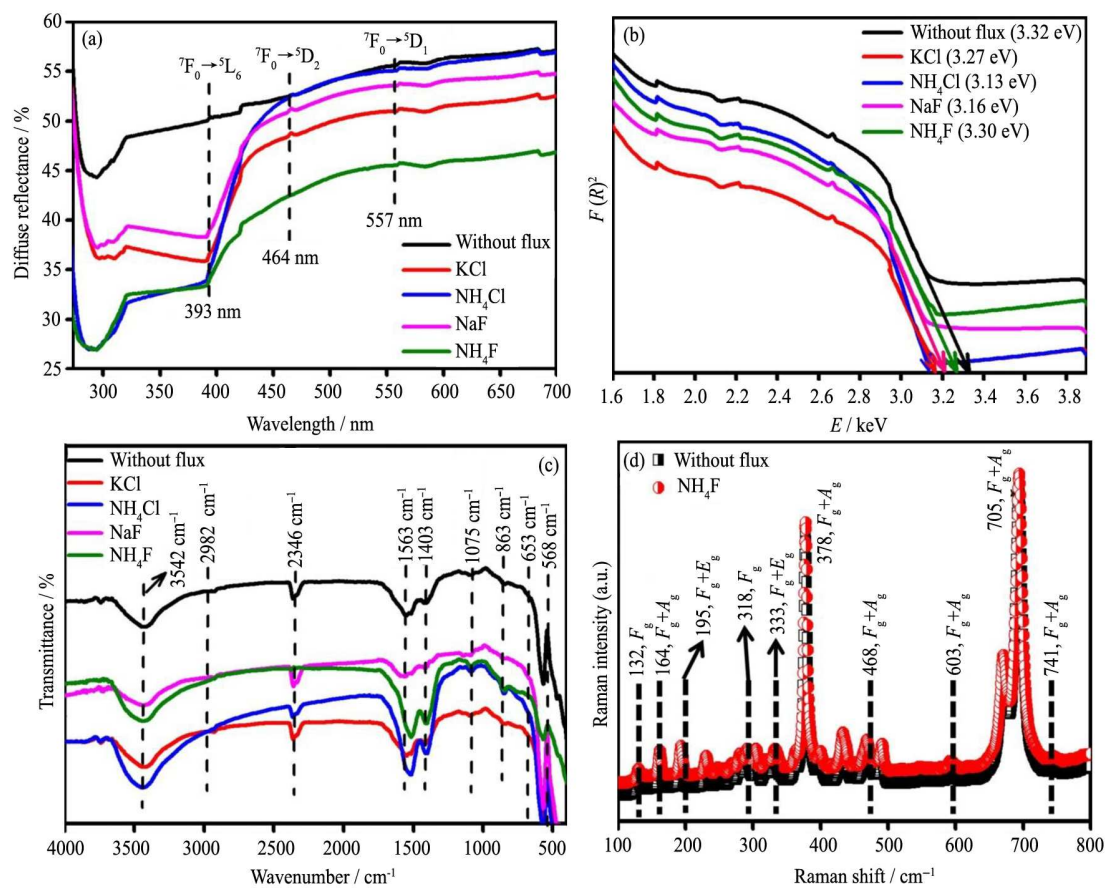
Fig.3 (a) DR spectra, (b) energy band gap plots, (c) FTIR spectra and (d) Raman spectra of Y$_2$O$_3$:Eu^{3+} (5 mol%) NPs without and with fluxes.
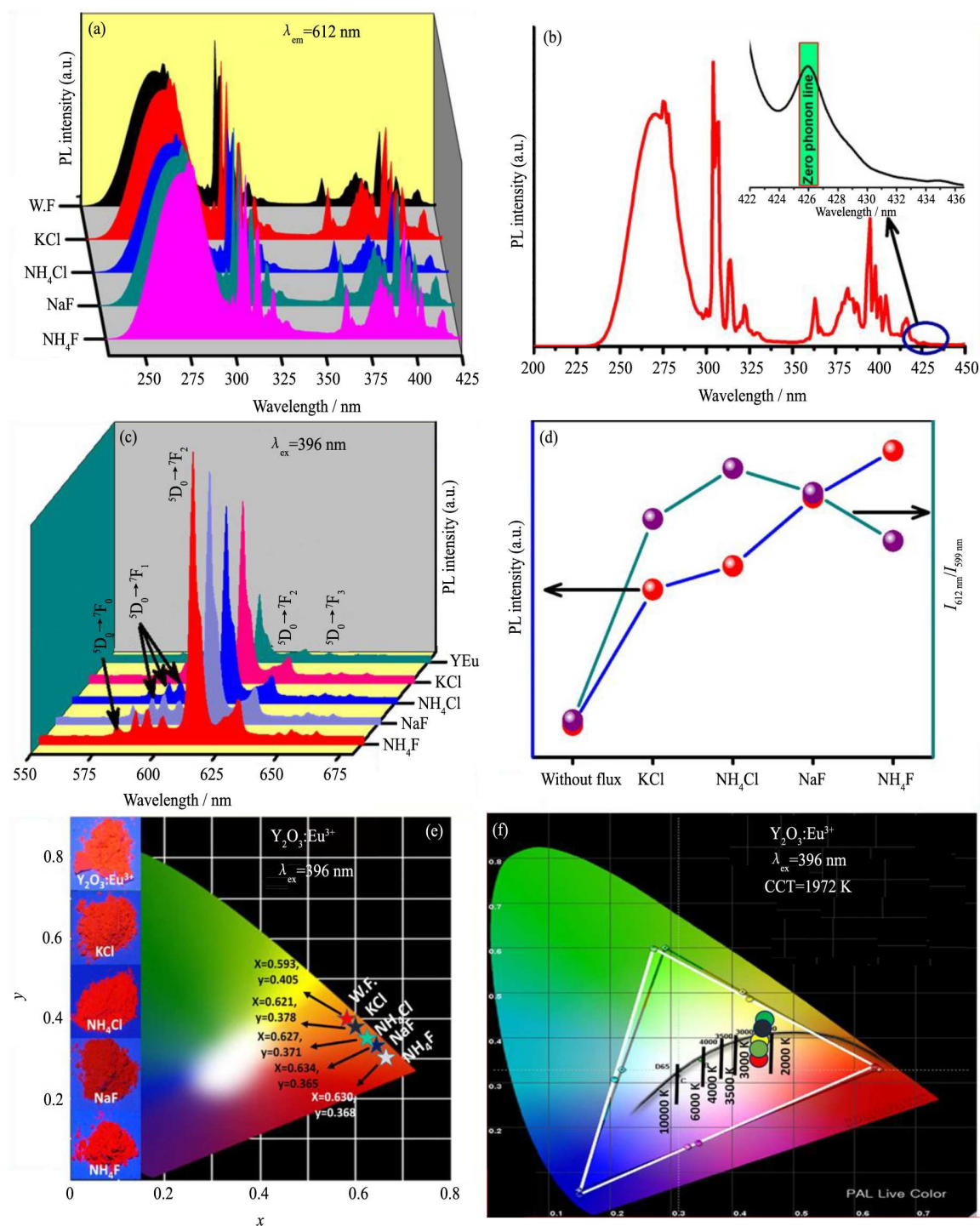
Fig.4 (a) Excitation spectra, (b) zero phonon spectrum, (c) emission spectra of Y_2O_3:Eu^{3+} (5 mol%) with and without various fluxes, (d) PL intensity and asymmetric ratio versus various fluxes and (e, f) CIE and CCT diagrams of Y_2O_3:Eu^{3+} (5 mol%) without and with different fluxes.
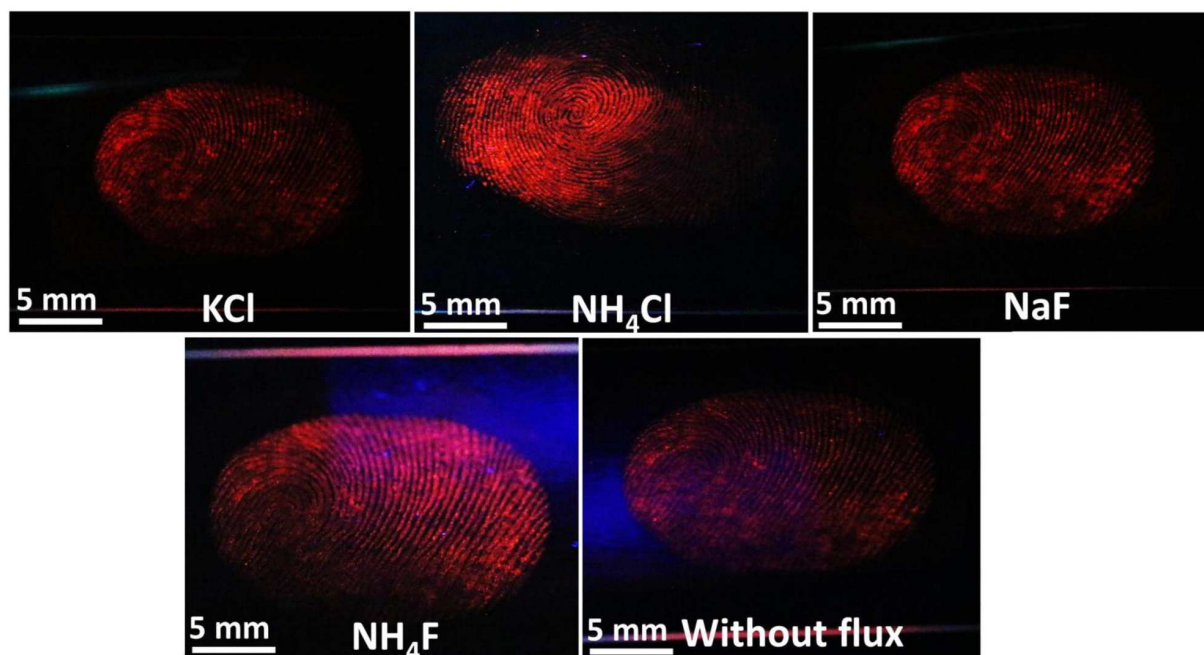
Fig.5. LFPs developed on the glass surface stained by optimized Y_2O_3:Eu^{3+} (5 mol%) NPs with and without various fluxes.
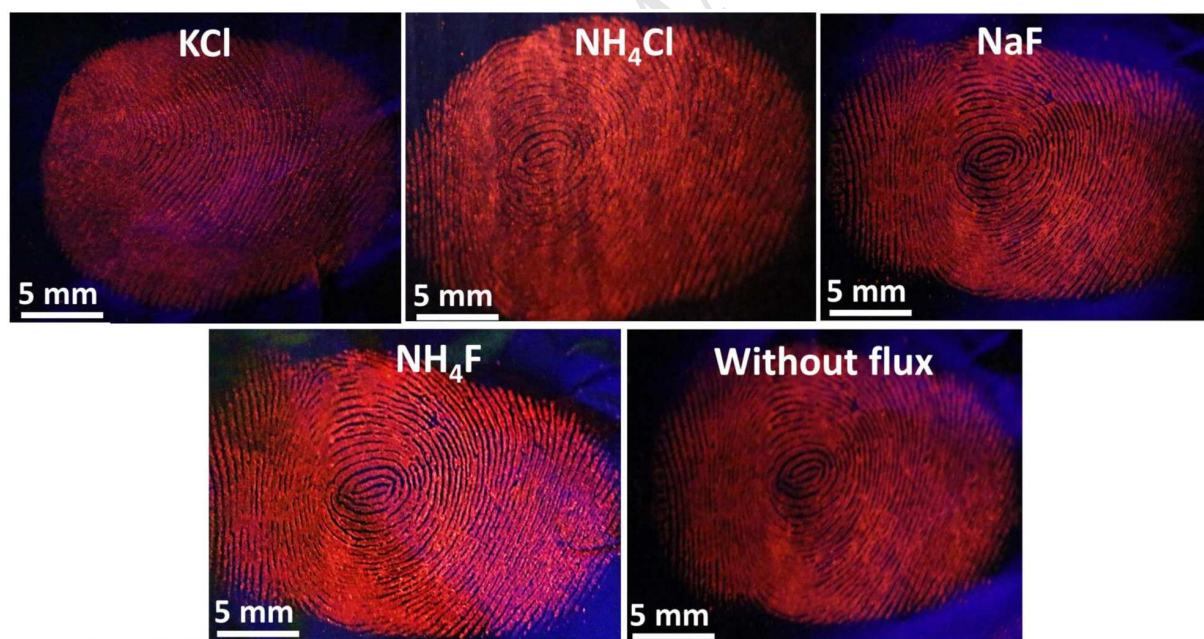
Fig.6. LFPs visualized on aluminium foil surface by using optimized Y_2O_3:Eu^{3+} (5 mol%) NPs without and with various fluxes.
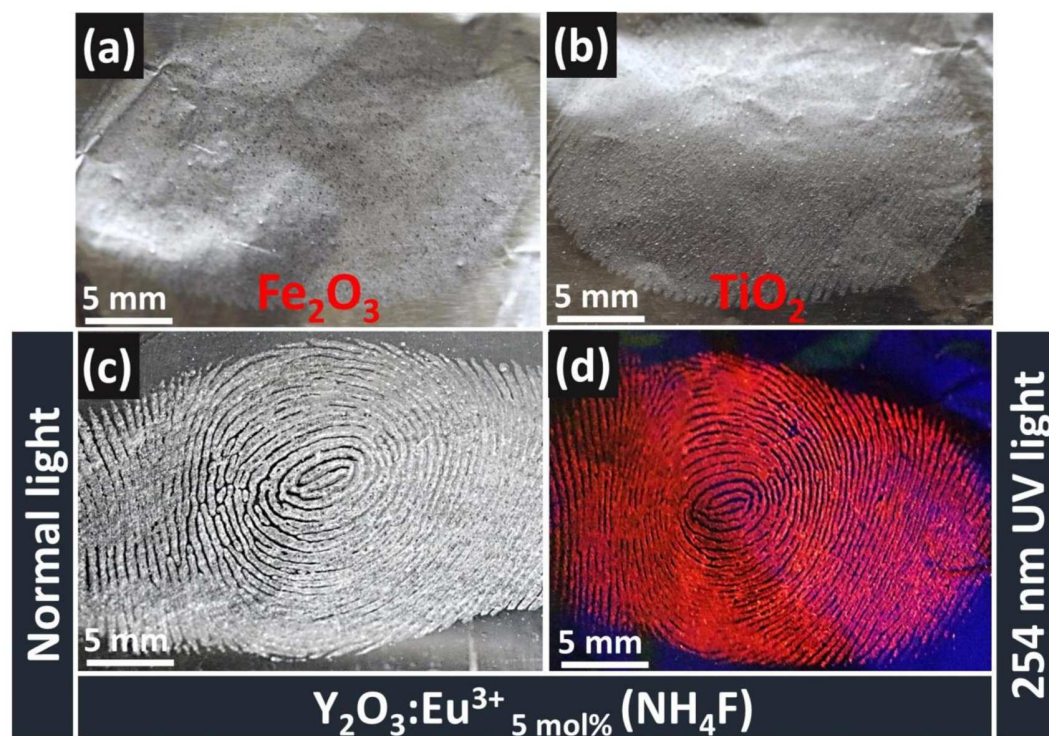
Fig.7. LFPs visualized by commercial powders including Fe_2O_3, TiO_2 and optimized NPs.
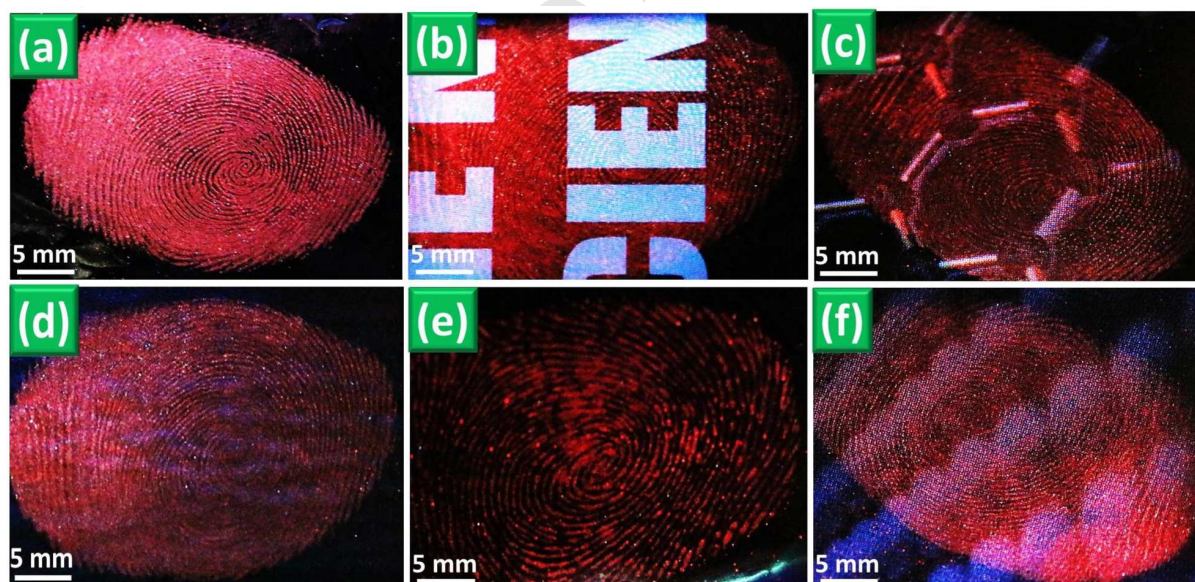
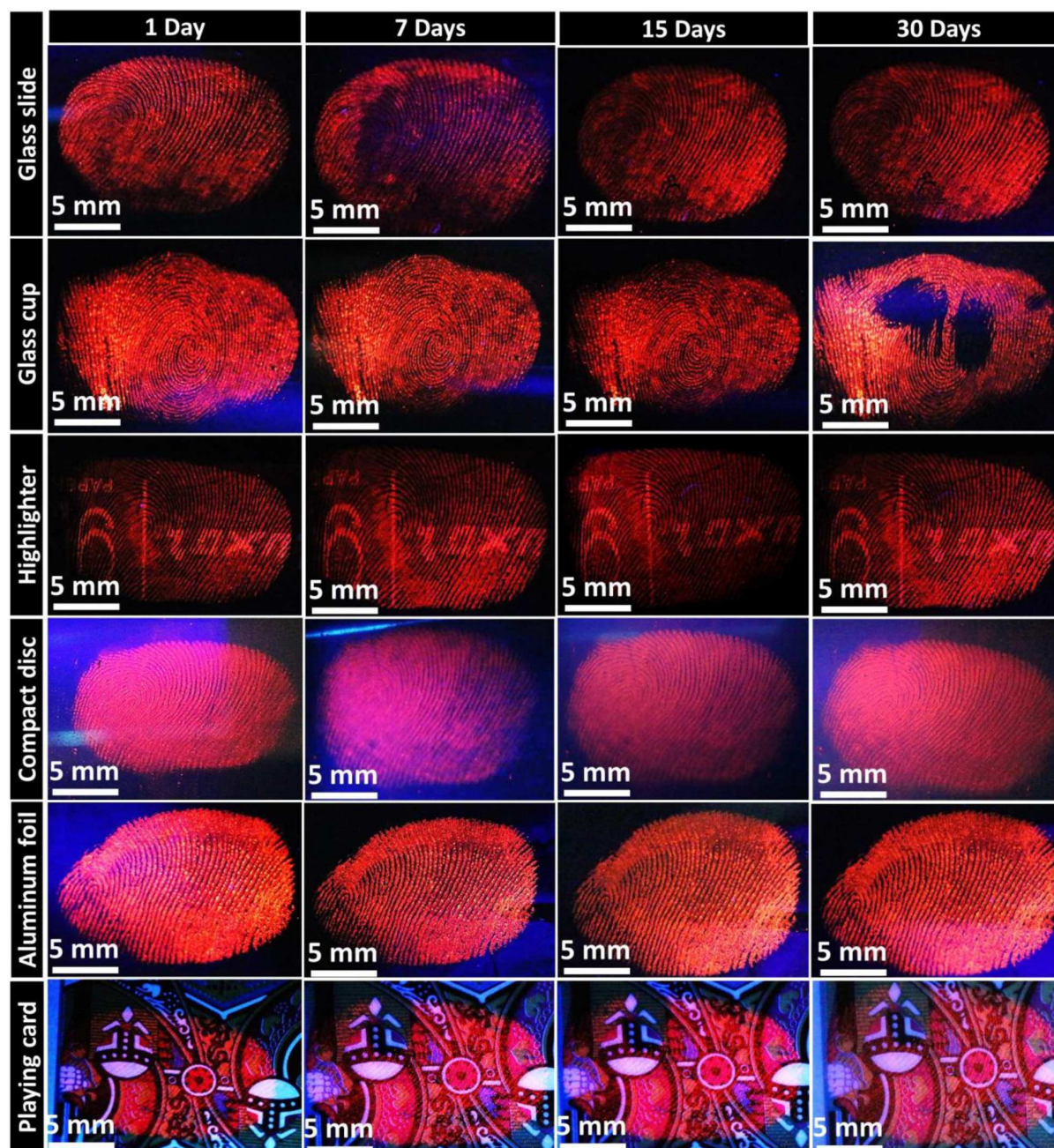Fig.8. Visualized LFPs by using optimized NPs on various porous surfaces under UV 254 nm light.

Fig.9. Aged LFPs recovery on non-porous and porous surfaces stained by optimized NPs under UV 254 nm light followed by powder dusting technique.
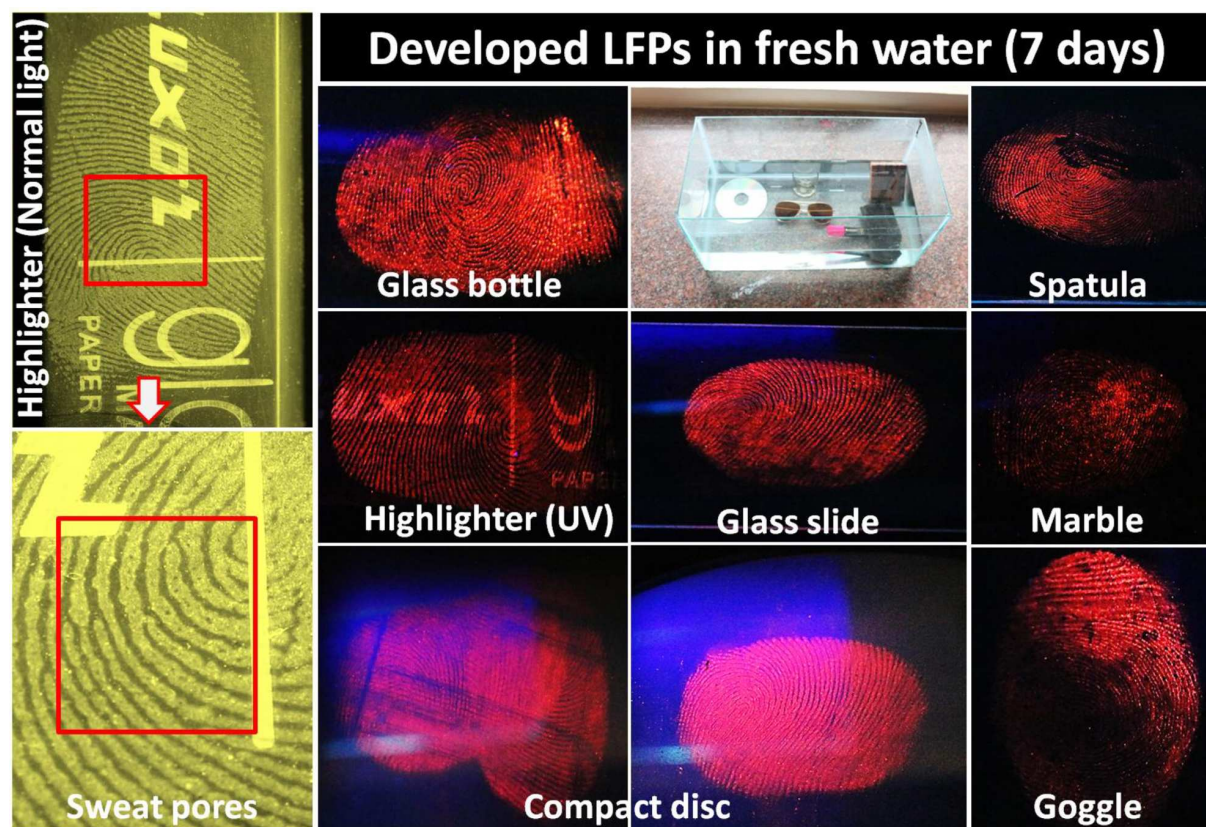
Fig.10. LFPs recovery using optimized NPs on the various non-porous surfaces treated with fresh water.

Table.1. Comparison of FP results obtained in the present study with those of reported data.

Host	Method of Synthesis	Types of surfaces used for detection	FP detection	FP aging	Effect of temperature	Abrasion test	Aquatic treatment
NaYF$_4$:Yb,Er	Solvothermal (180 °C/24 h)	Ceramic tile, marble, glass (non-porous) note papers, Chinese paper money, and plastic plates (porous)	Type I and II	-	-	-	-
Y$_4$Zr$_3$O$_{12}$:Eu^{3+}	Solvothermal (1000 °C/5 h)	Aluminum foil, plastic tube (porous) glass, compact disk, stainless steel (non-porous)	Type I and II	-	-	-	-
YVO$_4$:Eu, LaPO$_4$:Ce,Tb	Hydrothermal (180 °C/24 h)	Plastic cards, aluminum alloys sheets, printing papers (porous) ceramic tiles, marbles, painted wood, and floor (non-porous)	Type I and II	-	-	-	-
Fluorescent SiO$_2$ NPs	Stöber method	Glass (non-porous)	Type I and II	-	-	-	-
(PPV) NPs	Modified Wessling (80 °C / 3h)	Adhesive tape (porous)	Type I and II	-	-	-	-
Fluorescent semiconducting polymer dots	Suzuki coupling reaction (100 °C /48 h)	Printing paper and colored paper (porous) glass, aluminum foil, plastic bag, and acrylic sheet (non-porous)	Type I, II and III	-	-	-	-
AuNCs@MMT	One-pot microwave 35 °C under vacuum condition	Weighing paper, adhesive tape (porous) binder clips, slide glass, transparent tweezers and porcelain enamel (non-porous)	Type I, II and III	-	-	-	-
ESM-CaS NPs	Reverse microemulsion	Foil and plastic substrates (porous) tile and glass (non-porous)	Type I and II	-	-	-	-
Y$_2$O$_3$:Eu^{3+}, M$^+$ (M$^+$ = Li, Na, K)	Combustion (700 °C/3 h)	Porous Non-porous Semi-porous	Type I, II Type I, II, III Type I, II	1-30 d	30 – 50 °C	3 Cycles	7 d immersion

Graphic Abstract (TOC)
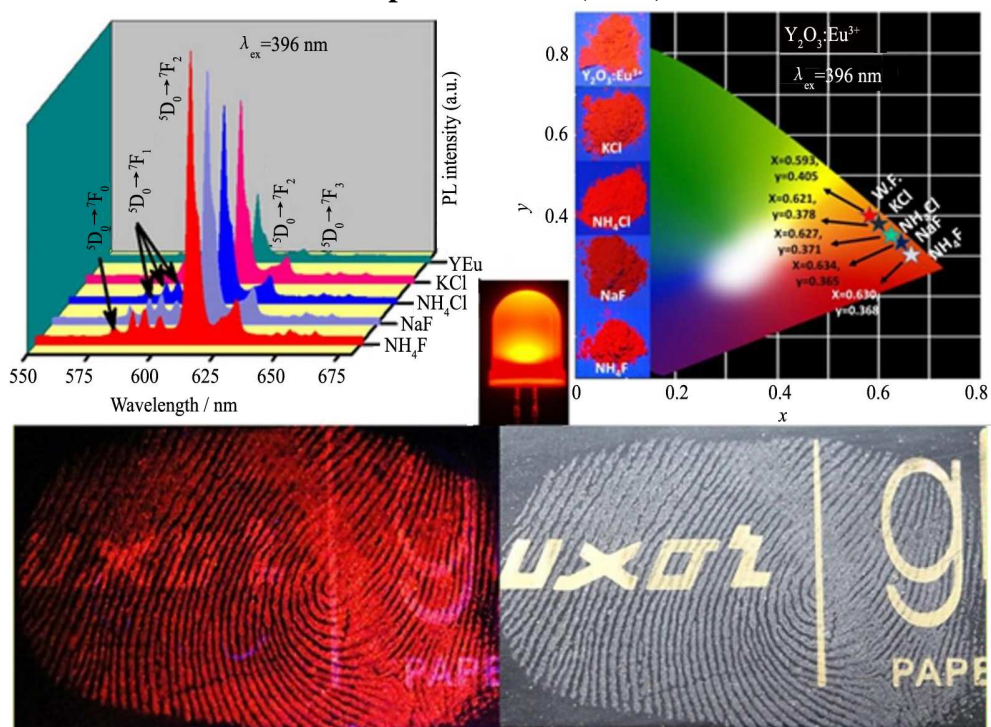
> ➤ Fluxes blended $Y_2O_3:Eu^{3+}$ NPswere prepared by facile solution combustion route.

> ➤ Optimized samples exhibitedas novel sensing agent for the visualization of LFPs.

> ➤ NH_4F flux blended NPs showed the highest PL intensity among the used fluxes.

> ➤ $Y_2O_3:Eu^{3+}$ NPs with NH_4F flux was suitable for forensic and LED's applications.

Supplementary Document for the manuscript No.: JRE-D-17-00545

Title: Flux blended synthesis of novel Y_2O_3:Eu^{3+} sensing arrays for highly sensitive dual mode detection of LFPs on versatile surfaces

Name of the Journal:-Journal of Rare Earths

The sharp and intense diffraction profiles of the prepared samples were well matched to body-centered cubic structure with space group Ia-3 and planes are good agreement with standard JCPDS file No. 41-1105. No obvious impurity peaks are observed which confirms the formation of single phase compound. A small peak shift at 2θ of ~ 29° corresponding to (440) plane is observed due to induced fluxes into the host Y_2O_3:Eu^{3+} (5 mol%) (Fig.S1 (b)).The crystallite size of the prepared samples is calculated using following Scherrer's relation [S1];

$$D = 0.9\lambda/\beta\cos\theta$$

------------------ (1)

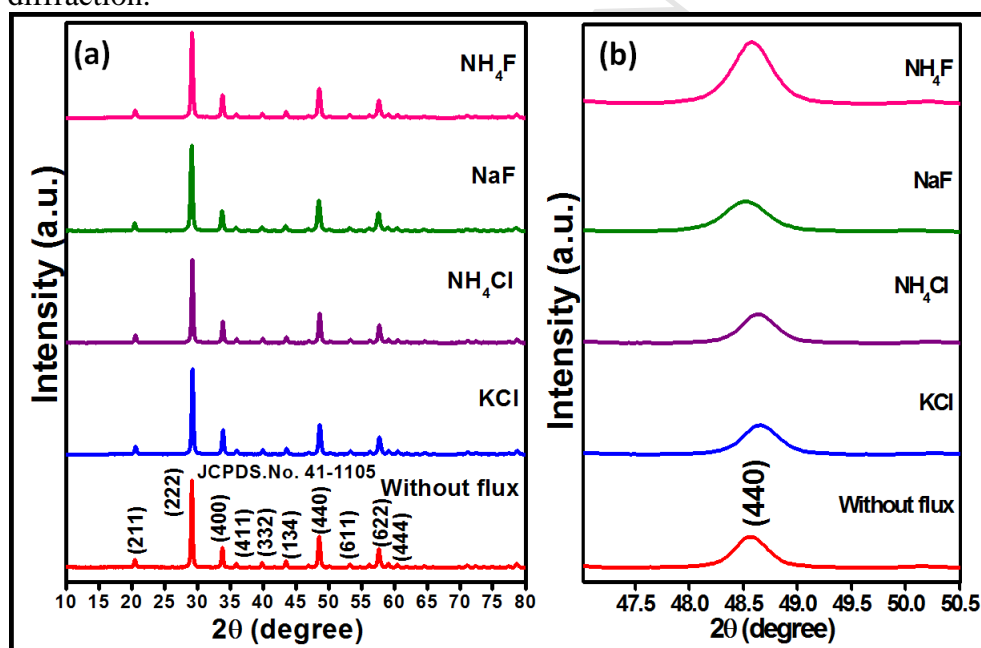where, λ ; wavelength of the X-rays, β ; the full- width at half maximum (FWHM) and θ ; angle of diffraction.

Fig.S1 (a) PXRD patterns of Y_2O_3:Eu^{3+} (5 mol%) NPs with different fluxes, (b) magnified image of a plane (440).

As shown in Fig.S2, detailed ridge characteristics namely level I - III are clearly revealed on spatula, highlighter and glass under both normal and UV 254 nm light. While the LFPs on the compact disc and goggle restricted to level 1 and 2 details due to background hindrance. Moreover, it is noteworthy that the LFPs developed on rough surfaced coin can also provided clear friction edges, demonstrating that our optimized NPs is highly efficient, versatile and can be applied to visualize LFPs on virtually all non-porous surfaces. However, in order to demonstrate the robustness of optimized sample for practical use, individual LFPs are visualized under both normal and UV 254 nm light on glass surface, as shown in Fig.S3.

Well defined three levels of FP ridge details namely, bifurcation, island, crossover, whorl, small ridge, eye, bridge, specialty and sweat pores (level III) are clearly visualized under dual illumination.
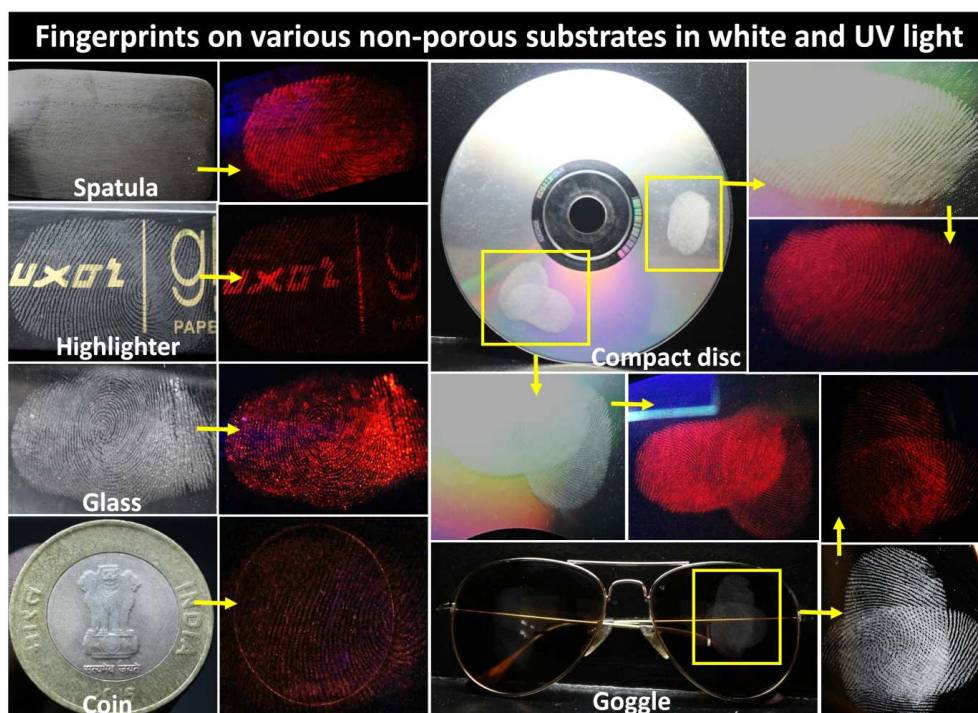

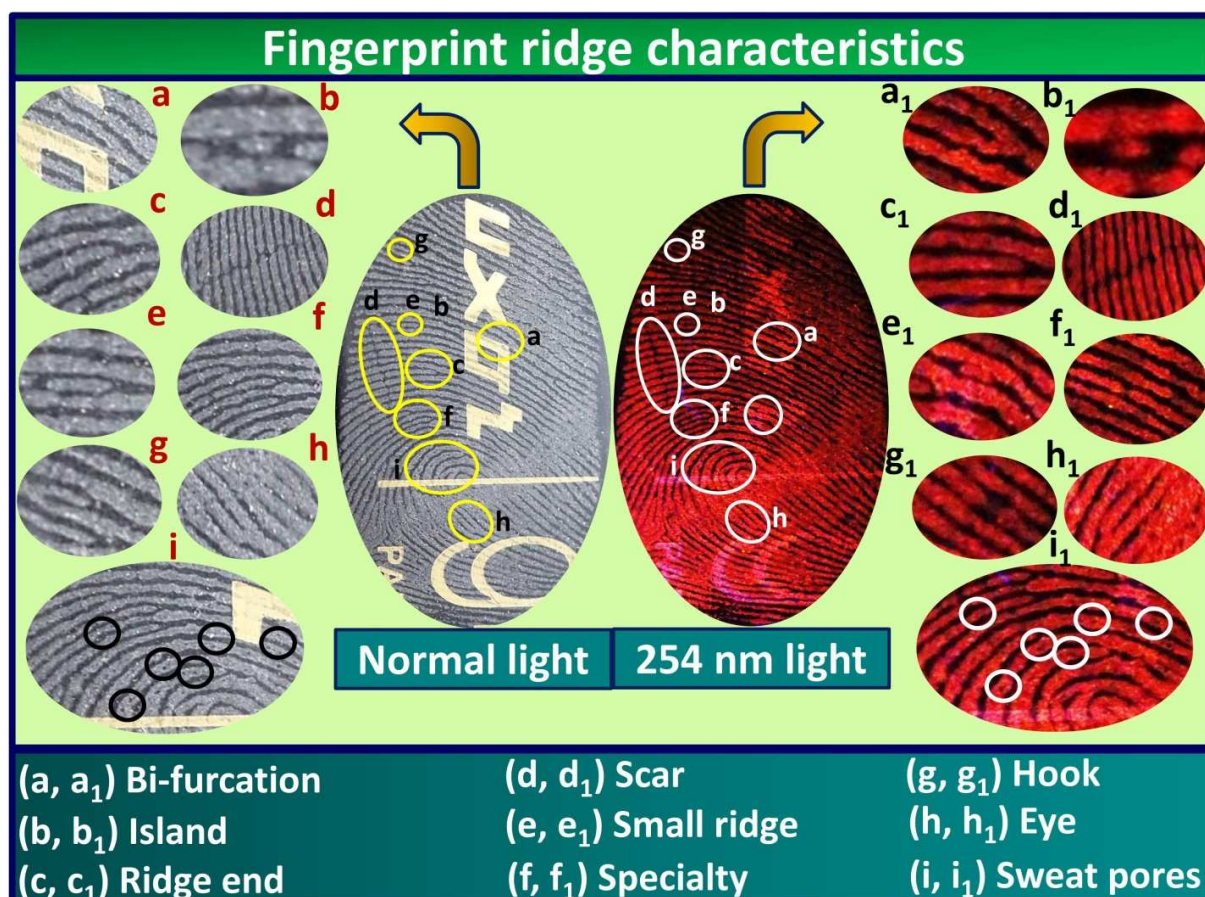Fig.S2. Visualized LFPs using NPs on various non-porous surfaces under white and UV 254 nm light.

Fig.S3. Various ridge details of individual FPs on glass surface under normal and UV 254 nm light.

These fruits and vegetables subjected to deterioration which depends on environmental and storage conditions (e.g., temperature and humidity) [S2]. As can be seen from the (Fig.12 (a' & d')) it is evident that the brinjal and green apple exhibit well defined ridges owing to its smooth and longer shelf life. Further, the visualized LFPs on capsicum, cucumber and watermelon are restricted to level I and II details due to high background hindrance. LFPs visualized on papaya exhibit indistinct ridge details due to the uneven surfaces (Fig.S4 (f')). The present results clearly demonstrated that the sensitivity of the prepared sample is high enough for visualization of LFPs on various neglected semi-porous surfaces.
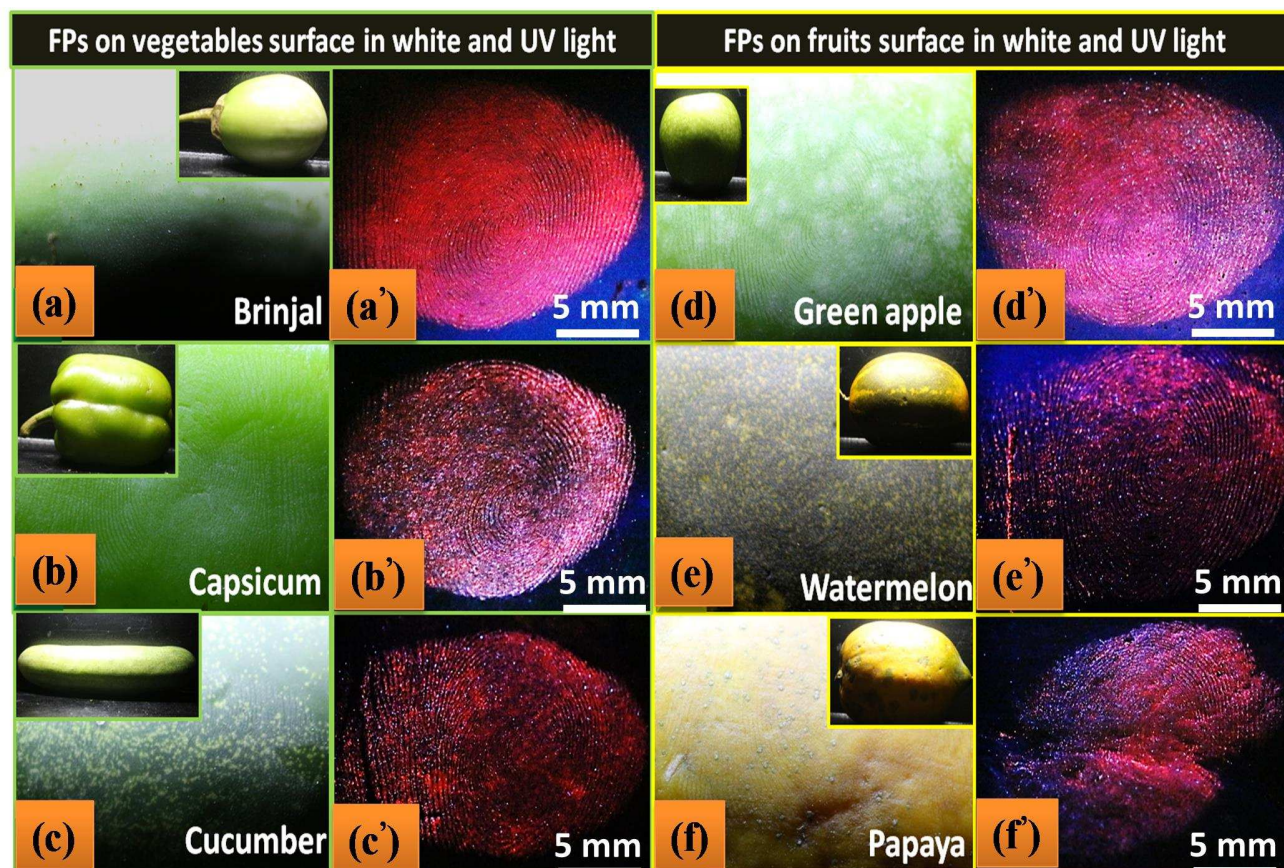
Fig.S4. LFPs visualized by the optimized NPs on various neglected vegetables and fruits surfaces.

Conversely, bare LFPs are maintained at various temperatures for ~ 10 min and afterwards stained by optimized NPs exhibits sharp well defined ridge characteristics and reveals level 1 and level 2 details upto 35 ^{o}C (Fig.S5) under UV 254 nm light.However, faint FP patterns were observed, when temperature was increases to 40 ^{o}C. Further, when the temperature was increased to 50 ^{o}C, the ridge patterns were completely disappeared due to evaporation of biogenic constituents of LFPs. The obtained result signifies the excellent reproducibility of the prepared sample.
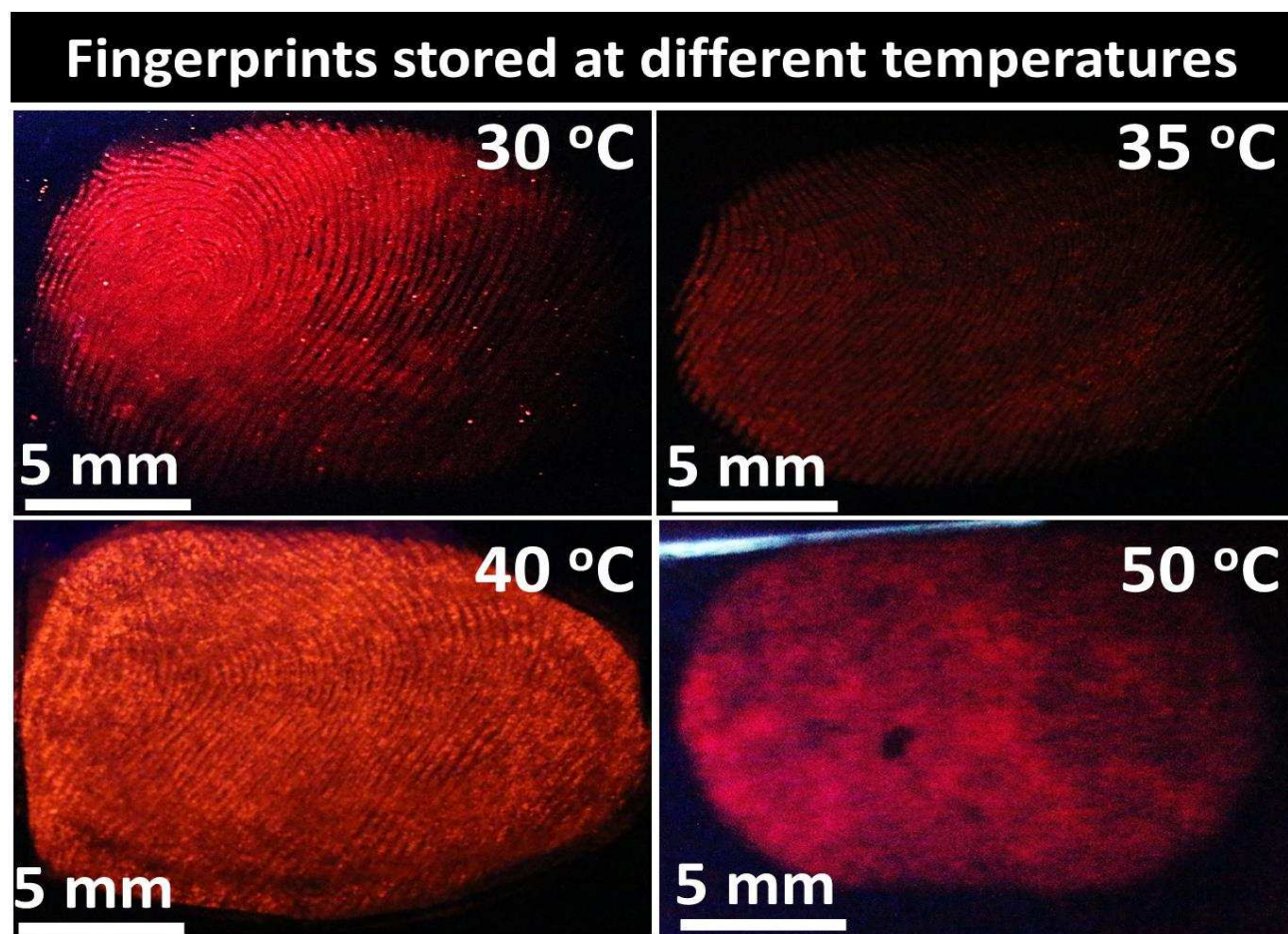
Fig.S5. LFPs on glass surface stored at different temperatures stained by optimized NPs.

Series of physical scratch test is performed on various surfaces including television remote, compact disc, granite and spatula before and after abrasion under 254 nm light to investigate external abrasions which can destroy LFPs (Fig.S6). The obtained results indicate that the visualized LFPs using prepared sample exhibits clear ridge details even after III scratch. These results validate the optimized NPs and powder dusting method is versatile and novel sensing colorimetric array for visualization of LFPs for forensic analysis.
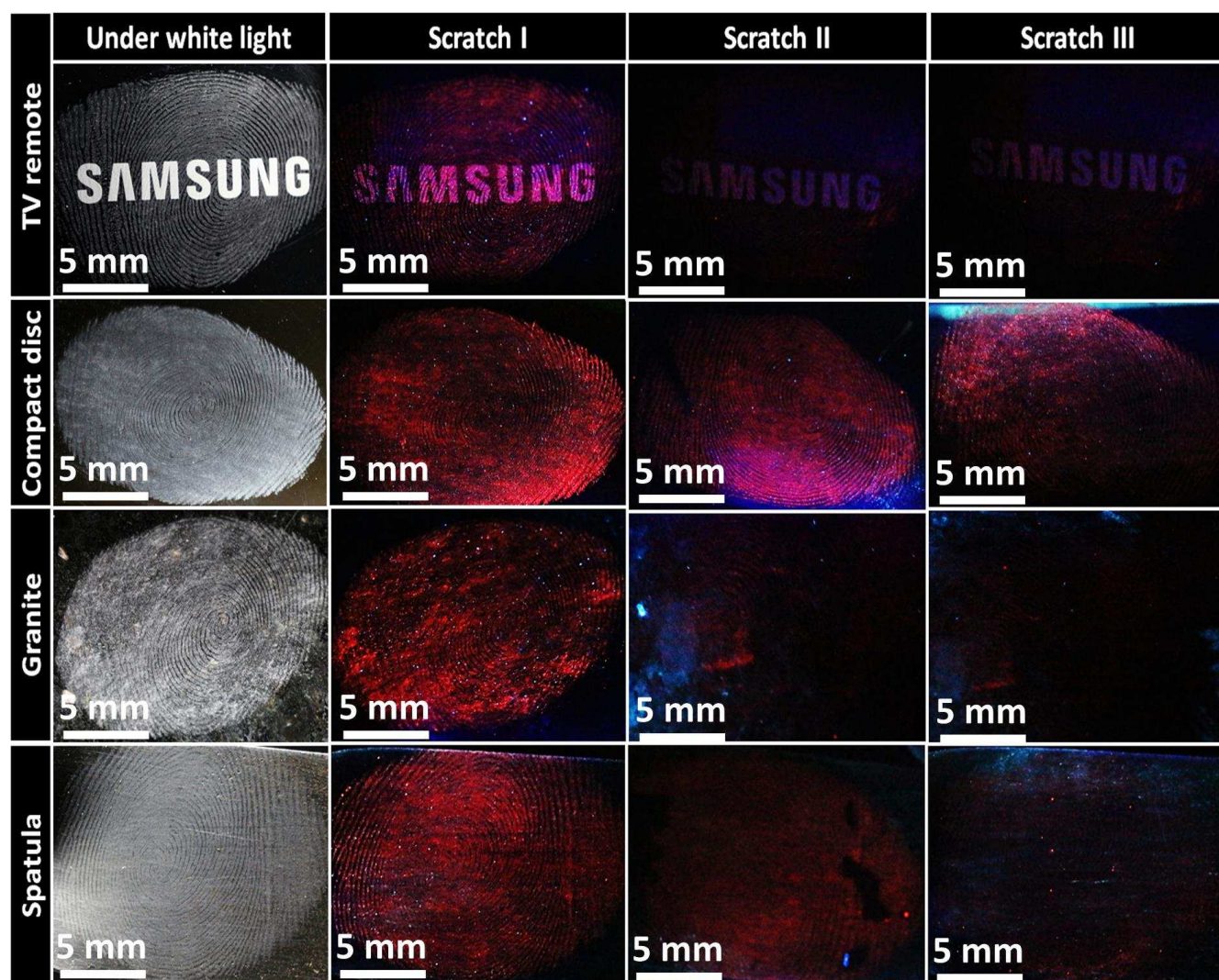
Fig.S6. Visualization of LFPs before and after scratch test using optimized NPs on various non-surfaces under normal and UV 254 nm light.

References for supplementary section:-

[S1] Saif M, Synthesis of down conversion, high luminescent nano-phosphor materials based on
new developed Ln^{3+}:$Y_2Zr_2O_7$/SiO_2 for latent fingerprint application. *J. Lumin.* 2013;135: 187.

[S2] Suresh C, Nagabhushana H, Darshan GP, Basavaraj RB, Kavyashree D, Sharma SC,

Arulmozhi A, Daruka Prasad B, AmithYadav HJ, FacileLaOF: Sm^{3+} based labeling agent

and their applications in residue chemistry of latent fingerprint and cheiloscopy under UV–

visible light, Arabian J. Chem. https://doi.org/10.1016/j.arabjc.2017.09.014.